ACS Photonics

pubs.acs.org/journal/apchd5

Letter

Bright High-Purity Quantum Emitters in Aluminum Nitride Integrated Photonics

Tsung-Ju Lu,*,‡ Benjamin Lienhard,‡ Kwang-Yong Jeong, Hyowon Moon, Ava Iranmanesh, Gabriele Grosso, and Dirk Englund*

Cite This: *ACS Photonics* 2020, 7, 2650–2657

Read Online

ACCESS | Metrics & More | Article Recommendations | Supporting Information

ABSTRACT: Solid-state quantum emitters (QEs) are fundamental in photonic-based quantum information processing. There is strong interest to develop high-quality QEs in III-nitride semiconductors because of their sophisticated manufacturing driven by large and growing applications in optoelectronics, high voltage power transistors, and microwave amplifiers. Here, the generation and direct integration of QEs in an aluminum nitride-based photonic integrated circuit platform is reported. For individual waveguide-integrated QEs, an off-chip count rate exceeding 6×10^4 counts per second (cps; saturation rate $>8.6 \times 10^4$ cps) is measured at room temperature under continuous-wave (CW) excitation. In an unpatterned thin-film sample, antibunching with $g^{(2)}(0) \sim 0.08$ and photon count rates exceeding 8×10^5 cps (saturation rate $>1 \times 10^6$ cps) are measured at room temperature under CW excitation. Although spin and detailed optical line width measurements are left for future work, these results already show the potential for high-quality QEs monolithically integrated in a wide range of III-nitride device technologies that would enable new quantum device opportunities and industrial scalability.

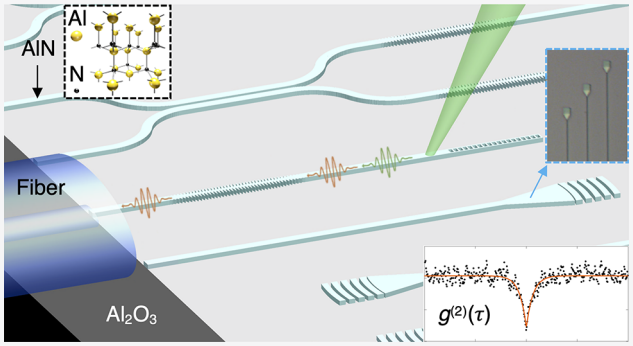

KEYWORDS: *thin-film aluminum nitride, quantum emitters, photonic integrated circuits, single photons, wide-bandgap semiconductors, quantum photonics*

Quantum emitters (QEs) with on-demand single photon emission are central building blocks for photonic-based quantum communication and quantum computation.[1,2] Over the past decade, crystal defect centers in wide-bandgap semiconductors have emerged as excellent solid-state QEs. In particular, a variety of color centers in diamond,[3−7] 4H silicon carbide (SiC),[8,9] and 6H SiC[10] have been demonstrated to have stable optical transitions coupled to long-lived spin ground states at room and cryogenic temperatures, resulting in spin-dependent single photon emission. The spin-photon interface provides access to electron spin states or indirectly to nuclear spin states, which can serve as quantum memories for quantum information processing[11,12] and quantum-enhanced sensing.[13]

Although these QEs in diamond and SiC have the leading properties among solid-state emitters, there is a lack of active chip-integrated photonic components and wafer-scale thin-film single-crystal diamond or SiC on low-index insulator, which limit the scalability of monolithic quantum information processing architectures in these materials. Hence, there is increased interest in exploring QEs in other material systems that can support both high-quality QEs and monolithic integration of wafer-scale photonic integrated circuits (PICs). Recently, alternative wide-bandgap materials, such as two-dimensional hexagonal boron nitride (2D hBN),[14] gallium nitride (GaN),[15] and aluminum nitride (AlN)[16] have attracted attention as potential host materials for quantum emitters due to their single-crystal heteroepitaxy of thin-film materials or the possibility to be integrated into any PIC platform in the case of 2D hBN.[17] Theoretical calculations show that AlN can serve as a stable environment for hosting well-isolated QEs with optically addressable spin states,[18] though experimental demonstrations of such QEs are outstanding. In contrast to diamond or SiC, which have strong covalent bonds, AlN is an ionic crystal with piezoelectric properties that may offer strain-based acoustic control for quantum spins.[19]

AlN is widely used in optoelectronics,[20] high power electronics,[21] and microelectromechanical systems,[22] resulting in a large, continuously expanding industry, bolstered by mature fabrication and growth technologies. AlN's optical transparency is bounded at the short-wavelength side by an exceptionally large bandgap of 6.015 eV (corresponding to ultraviolet) and extends

Received: August 8, 2020
Published: September 21, 2020

https://dx.doi.org/10.1021/acsphotonics.0c01259
ACS Photonics 2020, 7, 2650–2657

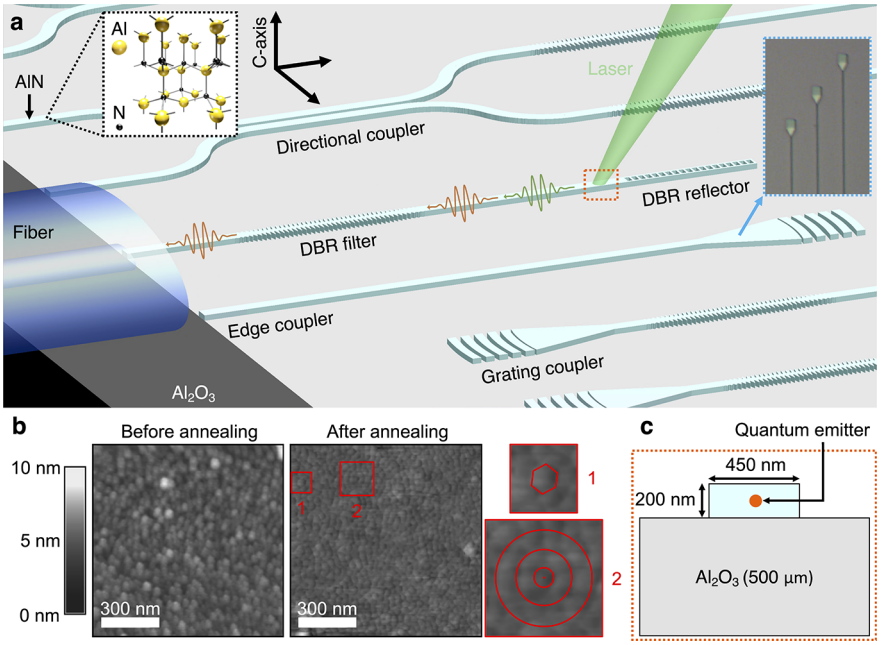

Figure 1. Quantum emitters in aluminum nitride integrated photonics. (a) Scalable AlN-on-sapphire photonic integrated circuits with integrated quantum emitters. Black inset: Wurtzite crystal structure of aluminum nitride (yellow: aluminum atom, black: nitrogen atom). Blue inset: Microscope image of the fabricated QE-integrated waveguides, where the grating couplers are used for visual feedback during fiber edge coupling. (b) Atomic force microscopy of a sample before and after annealing. Cut-out 1 indicates the hexagonal structure of the nanocolumns is maintained after annealing. Cut-out 2 shows slight coalescing of the AlN film columnar structure and improved orientation alignment to the *c*-axis, indicating an improved crystallinity to the AlN film. (c) Close-up cross-section of the single-mode AlN-on-sapphire waveguide, which is 450 nm in width by 200 nm in height. The quantum emitter is embedded within the AlN waveguide (not necessarily in the exact center as shown).

to the mid-infrared spectrum.[23] Its high thermal conductivity (κ = 285 W/m·K) and small thermo-optic coefficient (dn/dT = 2.32×10^{-5} K^{-1}) enable AlN devices to operate with long-term optical and physical stability.[24] The wide bandgap and the availability of highly crystalline AlN thin films grown on low-index sapphire substrates have enabled excellent AlN-based PIC platforms,[20,25] with a wide variety of nonlinear optical effects such as parametric frequency conversion,[26] sum/difference frequency generation,[27] electro-optic modulation,[24] and frequency comb generation.[27] Here we report on two types of bright room-temperature QEs emitting in the orange visible spectrum, integrated in a scalable AlN-on-sapphire PIC platform, as shown conceptually in Figure 1a, made possible by overcoming several material and processing challenges. Well-established fabrication processes for AlN PICs shown in previous works[17,25,28] enable engineering of QE-based quantum photonic devices tailored to any application needs.

RESULTS AND DISCUSSION

Material Processing and Quantum Emitter Creation in AlN. Our studies used wurtzite-phase AlN thin film on sapphire (Al_2O_3; Kyma Technologies, Inc.) with an AlN thickness of 200 nm. These samples were grown by plasma vapor deposition of nanocolumns (PVDNC) with a macro defect density of less than 10 per cm^2. The crystal orientation is along the *c*-axis (00.1 ± 0.2°), as indicated in the black inset in Figure 1a.

To create vacancy-based emitters, we ion-implanted the sample using a He ion microscope (Zeiss ORION NanoFab) at a He ion fluence of around 10^{15} ions/cm^2 with an accelerating voltage of 32 keV, followed by annealing in an argon environment at ambient pressure, which prevents AlN surface oxidation that occurs in ambient air at temperatures above 700 °C.[29]

We investigated different annealing recipes with maximum temperatures between 500 °C and 1000 °C. As seen from the atomic force microscope scans in Figure 1b, the 1000 °C annealing reduced the root-mean-square surface roughness 5-fold from 2.724 to 0.541 nm. The nanocolumns maintain the hexagonal crystal structure after annealing, indicated in the cutouts in Figure 1b, suggesting that the sample polytype remained wurtzite.

We characterized these samples by photoluminescence (PL) imaging in a confocal microscope setup using 532 nm laser excitation (Coherent Verdi G5 laser, power before the objective ~ 1 mW) through a 0.9 NA microscope objective (Nikon). The PL was filtered with a 560 nm long-pass filter and detected with avalanche photodiodes (APDs by Excelitas) via single mode fibers. These measurements showed a spatially uniform PL background, but no resolvable isolated QEs, for AlN samples annealed up to 700 °C; this background PL is reduced more than 100-fold and QEs are detectable in samples annealed at 1000 °C, which is the material processing condition used for the samples that are studied in the rest of this work.

The observed PL background reduction in combination with the lower surface roughness suggests an improved crystal structure, characterized by higher-uniformity nanocolumns. We tentatively attribute the reduced background to fewer unwanted defect centers in the bulk and on the surface of the material. In summary, the 1000 °C annealing is required for both suppression of the unwanted background photoluminescence as well as to facilitate the formation and activation of quantum emitters following He ion irradiation.

Spectral Analysis of Quantum Emitters. The room-temperature PL scan of a representative AlN sample after 1000 °C annealing (Figure 2a) shows a dark background with bright, micron-spaced bright spots. Analysis of the PL spectra, photon

https://dx.doi.org/10.1021/acsphotonics.0c01259
ACS Photonics 2020, 7, 2650−2657

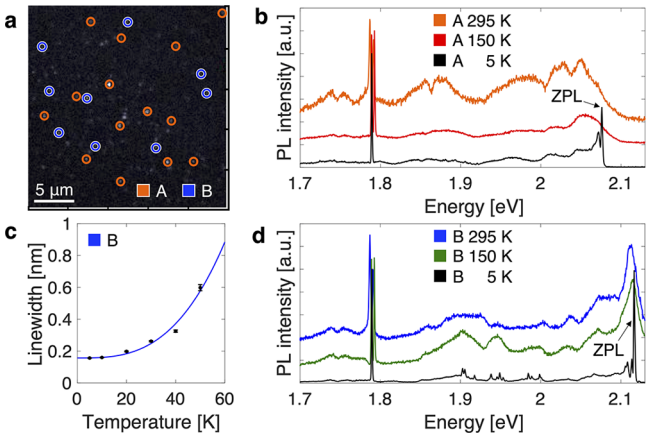

Figure 2. Spectral analysis of quantum emitters in thin-film w-AlN. (a) Quantum emitter density in a 25 μm × 25 μm area (white scale bar: 5 μm). Two types of emitters with orthogonal polarization states are identified, labeled as "A" and "B". (b) Temperature-dependent PL spectra of a representative type A quantum emitter (black, 5 K; red, 150 K; orange, 295 K), with the zero-phonon line (ZPL) indicated for the 5 K spectrum. (c) Temperature dependence of the type B quantum emitter's ZPL line width. (d) Temperature-dependent PL spectra of a representative type B quantum emitter (black, 5 K; green, 150 K; blue, 295 K), with the ZPL indicated for the 5 K spectrum.

statistics, emission lifetime, and polarization reveal these spots to be two orthogonally polarized classes of QEs labeled "A" and "B" (see Figure 3d), as detailed next.

At room temperature, both types of QEs emit in a broad spectrum covering from 580 to 650 nm, as seen in the curves labeled as 295 K in Figure 2b,d (spectra taken with Princeton Instruments Isoplane SCT320 spectrometer with a resolution of 0.07 ± 0.01 nm). The lines at 1.79 eV are caused by chromium ion-related impurities in sapphire[30] that we filter in following measurements with a 690 nm short-pass filter.

We performed low-temperature PL measurements to study phonon coupling characteristics in a closed-cycle helium cryostat (Montana Instruments) with a built-in confocal objective (NA = 0.9), and we used the same 532 nm laser for excitation and APDs for detection as previously stated. Figure 2b,d shows low-temperature PL spectra of a type A and B QE, respectively, at 5 and 150 K. While the type B emitter shows a resolvable zero-phonon line (ZPL) peak for all temperatures, the ZPL for the type A emitter is not resolvable and overlaps with the sideband at high temperatures (>30 K). Common to all 5 K spectra is a strong ZPL peak, accompanied by a red-shifted satellite peak.

The temperature dependence of the ZPL line width gives information about the interaction between the defects and host crystal lattice, as well as the emitter dephasing mechanisms. Figure 2c shows the temperature dependence of the emitter line width approximated from Lorentzian fits for a type B emitter. We determine a line width of 0.16 ± 0.01 nm at 5 K, which is not limited by the spectrometer resolution (~0.07 nm). A T^3 function fits the line width broadening with increasing temperature, similar to the silicon vacancy (SiV) and other defects in diamond.[31] The T^3 dependence results from field fluctuations caused by phonon-induced dislocations of crystal defects and color centers,[32] allowing us to conclude that these AlN QEs are point defects.

The Debye−Waller factor (DWF) indicates the extent of electron−phonon coupling for the emitter. We estimate it from DWF = I_{ZPL}/I_{TOT}, where I_{ZPL} is the ZPL PL emission and $I_{TOT} = I_{ZPL} + I_{PSB}$ is the total PL emission calculated by combining the ZPL PL emission I_{ZPL} with the phonon broadened PL I_{PSB}. Here, we fit the ZPL and PSB peaks with separate Lorentzian fit functions. At cryogenic temperatures, we determine the DWF to be 15 ± 2%.

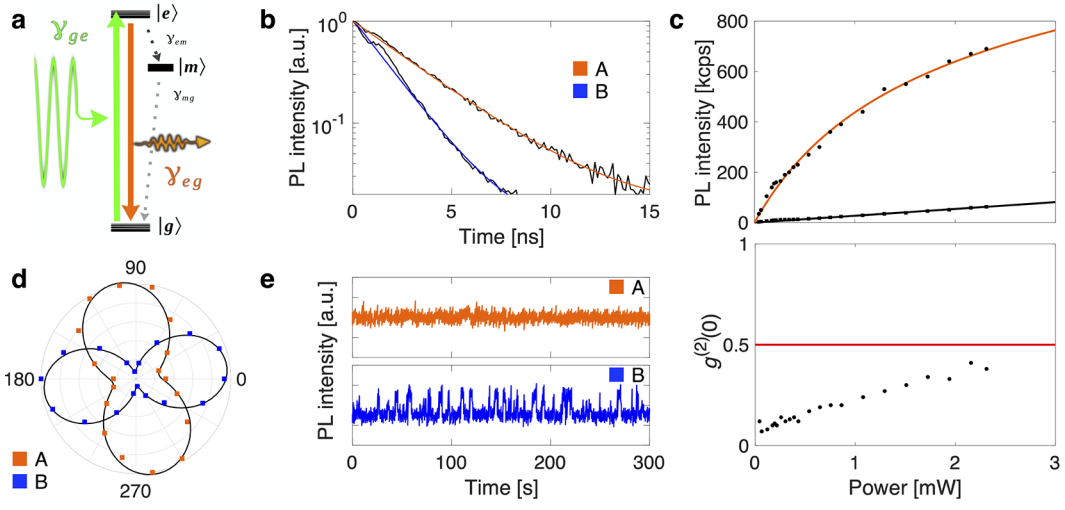

Figure 3. Photophysical properties of emitters. (a) Graphical illustration of a three-level system. (b) Excited state lifetime measurements fitted with a single exponential decay function, showing an excited state lifetime of 3.1 ± 0.1 ns for type A emitters (orange) and 1.7 ± 0.1 ns for type B emitters (blue). (c; Top) PL intensity saturation response of a type A emitter exceeding 1 million counts per second at saturation, with a saturation power of 1.5 mW (data with orange fit). The data with black fit shows the associated background. (Bottom) Plot of $g^{(2)}(0)$ as a function of excitation power, showing the high single photon emission purity up to twice the saturation power. Red line indicates the cutoff of $g^{(2)}(0) < 0.5$, indicating single photon emission. (d) Polar plots of PL as a function of linear excitation laser polarization. The emitters are split into two classes of emitters: one with a linearly oriented emission polarization orthogonal to the excitation spectrum (type A) and one with a linearly oriented emission polarization parallel to the excitation (type B). (e; Top) long-time photostability of a type A emitter. The emitter did not show any evidence of blinking or bleaching during the course of the experiments. (Bottom) photostability of a type B emitter, showing blinking at subsecond time scales.

https://dx.doi.org/10.1021/acsphotonics.0c01259
ACS Photonics 2020, 7, 2650−2657

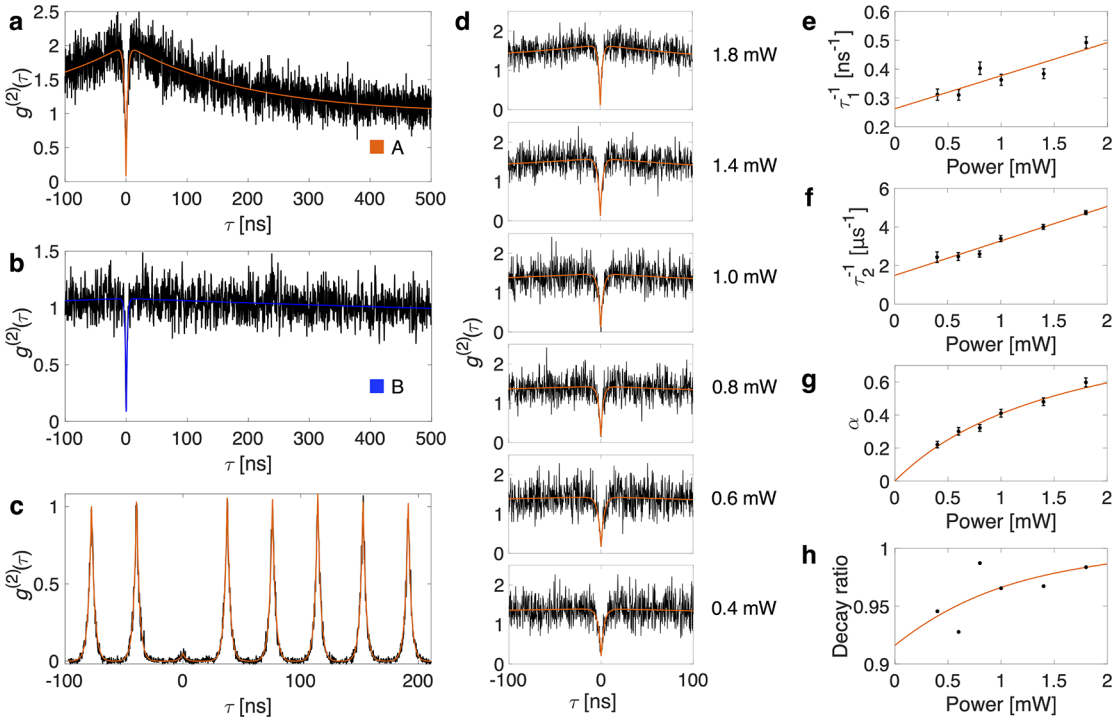

Figure 4. Photon statistics characterization of quantum emitters. Continuous wave excitation second-order autocorrelation histogram with (a) $g^{(2)}(0) = 0.08 \pm 0.06$ for a type A emitter and (b) $g^{(2)}(0) = 0.09 \pm 0.08$ for a type B emitter. (c) Pulsed excitation second-order autocorrelation histogram for a type A emitter with $g^{(2)}(0) = 0.05 \pm 0.002$. (d) Power-dependent second-order autocorrelation histograms for a type A emitter. Power-dependence of the reciprocal values of fitting parameters (e) τ_1 and (f) τ_2 in the second-order autocorrelation fits. The plots are linearly fitted (orange) and reflect the decay rates of the excited and metastable states, respectively. (g) Power-dependence of the fitting parameter α, which is representative of the nonradiative transitions via the metastable state. (h) Power-dependence of the decay ratio, which is defined as the ratio between the decay rate from the excited state to the ground state compared to the sum of all first order decay rates from the excited state.

Photophysical Characterization of Emitters. Next, we measured the fluorescence lifetime of our emitters. We can use the single exponential equation $I(t) \sim \exp(-t/\tau)$ for fitting the time-dependent PL intensity for the single state decay, in which τ represents the lifetime of the excited state. Figure 3b shows the excited state lifetime measurement using a pulsed excitation laser with a central wavelength of 532 nm, 10 nm bandwidth, pulse length of 1 ns, and 39 MHz repetition rate. The single-exponential fit indicates an excited state $|e\rangle$ lifetime of 3.1 ± 0.1 ns for the type A emitter and 1.7 ± 0.1 ns for the type B emitter.

Figure 3d shows the polar plots of the excitation-polarization-dependent PL intensity (without background subtraction) of both types of emitters fitted with a quadratic sinusoidal fit function $\sin^2(\theta + \phi)$, where the angular parameter θ represents the rotation of the linearly polarized pump laser and ϕ represents the orientation of the emitter relative to an arbitrary axis. Both types of emitters are shown to be single linearly polarized dipoles. Type A emitters have excitation and emission polarizations orthogonal to each other, while type B emitters have excitation and emission polarizations parallel to each other.

We also compared the photostability between the two types of emitters, using a 532 nm, 1 mW continuous-wave (CW) excitation over 5 min of continuous acquisition. As shown in Figure 3e, the type A emitters exhibited stable fluorescence emission over the course of more than 5 min without any blinking or bleaching. However, the type B emitter showed blinking at subsecond time scales.

Photon Statistics Characterization of Emitters. We measured the second-order autocorrelation photon statistics of the emitters with a Hanbury Brown Twiss (HBT) interferometer. Figure 4a,b shows the normalized second-order autocorrelation histograms for representative type A and B emitters, respectively, under 532 nm, 1 mW CW excitation at room temperature. The type A emitter has $g^{(2)}(0) = 0.08 \pm 0.06$, while the type B emitter has $g^{(2)}(0) = 0.09 \pm 0.08$, confirming that the emission is predominantly single-photon emission for both types of emitters ($g^{(2)}(0) < 0.5$). The histogram in Figure 4a indicates a strong bunching near $\tau = 0$, whereas the histogram in Figure 4b has weak bunching. This photon bunching feature suggests the presence of a dark metastable state. Figure 4c shows second-order autocorrelation histogram of a representative type A emitter under pulsed excitation at room temperature, with the laser set at a central frequency of 532 nm, 10 nm bandwidth, and 26 MHz repetition rate. Pulsed excitation resulted in a further improved single photon purity of $g^{(2)}(0) = 0.05 \pm 0.002$.

A typical two-level model does not explain the bunching behavior near $\tau = 0$ in the second-order autocorrelation histograms. We therefore adopt the next-simplest level diagram shown in Figure 3a: a three-level system with pump-power-dependent transition rates. This models the essential features we observe and allows a comparison with other well-studied emitters. Equation 1 shows the three-level model for fitting the experimental $g^{(2)}(\tau)$ data:

$$g^2(\tau) = 1 - (1 + \alpha)\exp\left(-\frac{|\tau|}{\tau_1}\right) + \alpha \exp\left(-\frac{|\tau|}{\tau_2}\right) \quad (1)$$

where τ_1, τ_2, and α are the excited state lifetime, metastable state lifetime, and fitting parameter. Figure 4d shows the power-dependent second-order autocorrelation histograms for a type A emitter, which are used to evaluate the electron dynamics. We

https://dx.doi.org/10.1021/acsphotonics.0c01259
ACS Photonics 2020, 7, 2650−2657

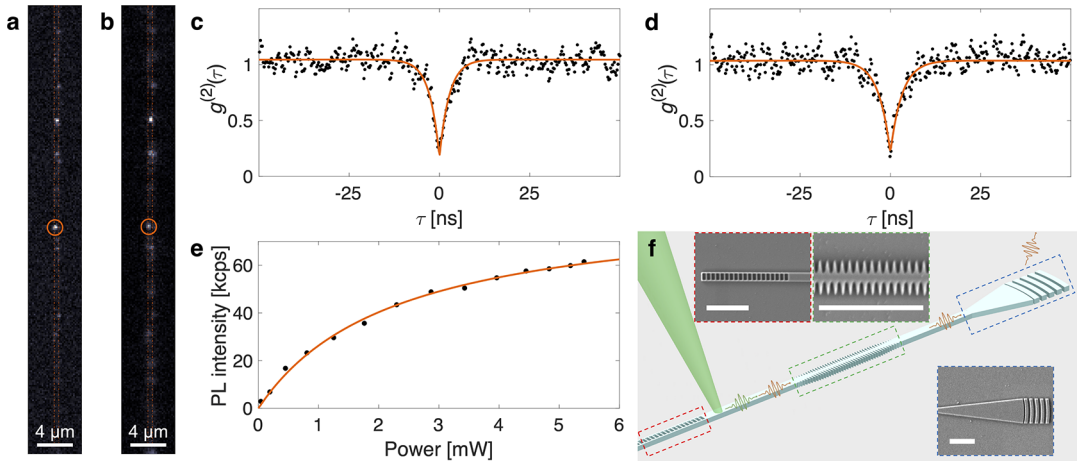

Figure 5. Photonic integration of emitters. Confocal PL scan of an AlN waveguide populated with quantum emitters throughout, with (a) confocal collection and (b) waveguide collection for detection. The circled emitter is the emitter that is studied in the photon-intensity correlation measurements. (c) Cross-correlation measurement of the emitter under 532 nm excitation between the photons collected via the confocal setup and the photons collected through the waveguide, with $g^{(2)}(0) = 0.17 \pm 0.07$, confirming the photons collected from the waveguide while exciting the emitter originates from the emitter. (d) Autocorrelation measurement of the emitter via waveguide collection only, with $g^{(2)}(0) = 0.21 \pm 0.08$. (e) PL intensity saturation response of an emitter with waveguide collection, with counts exceeding 8.6×10^4 cps at a saturation power of 2.3 mW. (f) Conceptual diagram of an AlN PIC with distributed Bragg reflectors as filter (green) and directional reflector (red), as well as a grating coupler (blue) for the dense population of read-out channels on the chip. Insets are SEM micrographs of the fabricated structures, with scale bars in each being 2 μm.

mainly focus on a type A emitter for these measurements due to its photostability compared to type B emitters, as shown in Figure 3e.

Fitting parameter τ_1 describes a two-level system, represented by the sum of the transition rates of an electron between the ground state and a single excited state:[8,33]

$$\frac{1}{\tau_1} = \gamma_{ge} + \gamma_{eg} \tag{2}$$

where γ_{ge} is the excitation rate from the ground state $|g\rangle$ to the excited state $|e\rangle$ and γ_{eg} is the radiative decay rate from the excited state $|e\rangle$ to the ground state $|g\rangle$, as shown in Figure 3a. Figure 4e shows a plot of $1/\tau_1$ versus excitation power, which can be linearly approximated as indicated by the orange fit. τ_1 at zero excitation power gives the lifetime of the excited state.[33,34] Hence, the linear fit in Figure 4e yields a lifetime of about 3.8 ns. The lifetime value extrapolated from the power-dependent $g^{(2)}(\tau)$ measurements is consistent with the measured lifetime of the type A emitter (Figure 3b), supporting that a three-level system is a suitable model for the type A emitters.

The second fitting parameter τ_2 describes the metastable state behavior, represented by a sum of the nonradiative decay rate from the excited state $|e\rangle$ to the metastable state $|m\rangle$ (γ_{em}) and the nonradiative decay rate from the metastable state $|m\rangle$ to the ground state $|g\rangle$ (γ_{mg}):[8,33]

$$\frac{1}{\tau_2} = \gamma_{em}\frac{\gamma_{ge}}{\gamma_{ge} + \gamma_{eg}} + \gamma_{mg} \tag{3}$$

τ_2 at zero excitation power gives the lifetime of the metastable state, which we found from the fit in Figure 4f to be about 673 ns.

The last parameter α, plotted as a function of excitation power in Figure 4g, is representative of the amount of bunching caused by the metastable state nonradiative transition. Mathematically, α is a product of the electron excitation probability and the probability of the subsequent decay to the metastable state:[8,33]

$$\alpha = \frac{\gamma_{ge}}{\gamma_{ge} + \gamma_{eg}}\frac{\gamma_{em}}{\gamma_{mg}} \tag{4}$$

The stronger the bunching, the higher the probability of intersystem crossing. Furthermore, the smaller the α, the more the emitter behaves as a two-level system.

Figure 4h shows as a function of excitation power the decay ratio, defined as the ratio of the decay rate from the excited state to the ground state versus all first order decay rates from the excited state (decay rate from the excited state to the ground state and decay rate from the excited state to the metastable state). The decay ratio from the excited state to the metastable state is constant for an ideal three-level model. Our experimental decay ratio versus power agrees with that, showing that the three-level system describes the type A emitter well and higher order level transitions can be neglected.

We next measured the PL intensity of the emitters as a function of the excitation power (with optimized polarization) to find the emitters' maximum emission count rates. We used a second room-temperature confocal microscope setup for these measurements, designed for efficient PL collection, by using a Nikon 1.3 NA oil immersion objective for excitation and collection, as well as using a dichroic filter with a 552 nm cutoff wavelength and a 560 nm long-pass filter to remove the excitation laser and Raman lines. Figure 3c (top) shows the saturation behavior of a type A emitter and the associated background.

Equation 5 describes the typical function for fitting the emission count rate I as a function of the measured excitation power P for a three-level system:

$$I(P) = I_\infty\frac{P}{P_{sat} + P} + \alpha P + \beta \tag{5}$$

where I_∞ is the emission count rate at saturation, P_{sat} is the excitation power at saturation, α is the linear power-dependent background slope, and β is the constant dark counts. We use eq 5 to fit the intensity saturation behavior measurement plotted in Figure 3c (top), which shows that the PL intensity exceeds 1 ×

https://dx.doi.org/10.1021/acsphotonics.0c01259
ACS Photonics 2020, 7, 2650−2657

10^6 cps at saturation, with a saturation power of 1.5 mW. Figure 3c (bottom) shows the $g^{(2)}(0)$ of the corresponding second-order autocorrelation measurements for each of the excitation powers used in Figure 3c (top), indicating single photon emission characteristics for the emitter up to excitation powers of 3 mW or twice the saturation power.

Photonic Integration of Emitters. Next, we created these QEs in AlN-on-sapphire PICs fabricated by a combination of electron beam lithography and dry etching (see Methods). The blue inset in Figure 1a is a microscope image of the fabricated QE-integrated waveguides coupled off chip with edge couplers; the grating couplers are used for visual feedback during fiber edge coupling. Using the same room-temperature confocal microscopy setup with a 0.9 NA objective described above for laser excitation, we used a cleaved Nufern UHNA3 fiber mounted on a XYZ piezo stage for edge-coupling to the AlN edge couplers, as illustrated conceptually in Figure 1a. Our edge coupler design was not optimized to mode match with the UHNA3 fiber. We expect the experimental coupling efficiency to be less than 7% due to it being sensitive to the edge coupler polishing quality.[28]

The confocal PL scan in Figure 5a with a confocal collection for detection of an AlN waveguide indicates QEs throughout, while Figure 5b shows the same confocal PL scan with a waveguide edge coupler collection into the UHNA3 fiber for detection. A comparison between the scans shows that all emitters are coupled into the waveguide. We use the circled emitter for the subsequent photon intensity correlation measurements.

We observe strongly antibunched emission from waveguide-coupled emission (Figure 5d) and cross-correlation measurements (top versus waveguide collection, Figure 5c) with 532 nm, 1 mW CW excitation at room temperature without background correction. Despite the rather low estimated edge-coupling efficiency of 7%, we observe a high count rate exceeding 6×10^4 cps out of the waveguide (Figure 5e), with 8.6×10^4 cps at a saturation power of 2.3 mW.

We show in Figure 5f several exemplary devices realized on the same AlN-on-sapphire platform, though not characterized in this study. Distributed Bragg reflectors can be used as directional reflectors (red boxes) to direct all the emission toward one side of the photonic circuit, as well as spectral filters (green boxes) to filter out excitation light that is scattered into the waveguide. After the spectral filter, the emission can be either first split by an on-chip beamsplitter or directly coupled off the chip via edge couplers or grating couplers that can be placed anywhere throughout the chip (blue boxes).

CONCLUSION

While we observed the formation of the QEs after He-ion implantation and annealing, both type A and type B QEs are also observed for samples that did not undergo He-ion implantation, albeit at a lower density, making it likely that the emitter type is either intrinsic or vacancy-based. Some sort of marker indicators on the bulk sample that are inert and do not degrade with the material treatments are needed to do a more careful study on the He-ion dose's effect on the QE formation and properties. As our emitters are in a 200 nm thick AlN film, we speculate from their stronger blinking behavior that type B emitters may be closer to the surfaces.[14]

While the three-level system in Figure 3a is a suitable model for fitting to the measurements of our emitters, we note that there are other possible explanations for the bunching behavior near $\tau = 0$ for our emitters' second-order autocorrelation histograms. Finding the origin of the emitters in future works would be necessary to conclusively explain the cause for this bunching behavior near $\tau = 0$. There have been many previous works reporting on quantum emitters in other nitride materials with emission wavelengths covering a wide wavelength range similar to the emitters in this work.[14,15,35,36] However, even with extensive theoretical density functional theory (DFT) modeling, the origin of these other emitter defects is not fully understood.[37] Our QEs in thin-film AlN offer insights and potential future research directions to reveal the origins of similar QEs that have been observed in both monolayer and microns thick bulk nitride materials, such as the possibility of direct 3D atomic reconstruction by scanning transmission electron microscopy.[38]

In conclusion, we demonstrated quantum emitters in a 200 nm thin-film AlN grown on top of sapphire, with count rates exceeding 1 million cps at saturation and high purity even at room temperature. We also showed that these QEs can be readily integrated in AlN-on-sapphire PICs using conventional AlN fabrication processes for patterning photonic components. While further studies are needed to investigate the predicted spin-dependent transitions coupling to spin qubits, strain-driven spin control, and other avenues toward spectrally narrower emission, the integration of stable QEs into AlN-on-sapphire PICs already opens the prospect of stable single photon sources integrated monolithically with optical modulators,[24] AlN-integrated single photon detectors,[39] and frequency conversion devices.[40] Furthermore, this work shows the potential of integrating high-quality QEs to a wide range of technologies comprised of the aluminum gallium nitride (AlGaN) family of materials that, thanks to their exceptional optical and electronic properties, as well as a large and growing industrial base, already form the state-of-the-art for applications in UV lasers, piezoelectric actuators and filters, high-power and high-speed electronics, and solid state lighting.[41−43]

METHODS

Material Processing. We ion-implanted the samples using a He ion microscope (Zeiss ORION NanoFab) at a He ion fluence of around 10^{15} ions/cm^2, with acceleration voltage of 32 keV, similar to previous methods for creating isolated defects in hBN.[44] We found that this He ion implantation by itself significantly increased the overall AlN PL but did not increase the detectable emitter density. Instead, annealing the AlN samples after He ion implantation creates resolvable photostable QEs. Each sample is annealed in an ambient pressure argon environment. The sample is increased with a slope of 2 °C/s under continuous gas flow. The temperature is kept constant for 30 min once the maximum defined temperature is reached before cooling down to room temperature again. The samples do not reveal any isolated QEs due to a resulting spatially uniform background fluorescence after annealing up to 700 °C. The background PL intensity decays exponentially in time when optically pumping the material with the 532 nm excitation laser. Increasing the maximum annealing temperature yields faster exponentially decaying background fluorescence under optical excitation. Isolated and photostable QEs start being detectable at annealing temperatures above 800 °C.

AlN Photonics. Development of integrated photonic circuits relies on the use of thin-film high-index material on a low-index substrate. As we show that our material treatment results in the creation of high-purity quantum emitters in a thin AlN film with just 200 nm thickness, we further investigate whether the

https://dx.doi.org/10.1021/acsphotonics.0c01259
ACS Photonics 2020, 7, 2650−2657

emitters can survive nanofabrication processes and be integrated with PICs. After emitter formation using the He ion implantation and annealing procedures described above, we fabricated PICs into the AlN thin film by using the electron beam lithography and chlorine reactive ion etching process developed previously.[25] Then, S1813 photoresist served as a protective layer for mechanical edge polishing. We diced the chip using an automatic dicing saw (DISCO DAD-3240) and polished the chip to produce optical-grade facets for edge coupling (Allied MultiPrep Polishing System 8). Finally, sonication in *N*-methyl-2-pyrrolidone (NMP) removes the S1813 protective layer and debris caused by dicing and mechanical polishing.

Experimental Setup. The room-temperature characterizations were performed using a confocal microscope. A green 532 nm laser (Coherent Verdi G5 laser) was used for excitation, with photoluminescence scans taken with a galvanometer mirror scanner in a 4F configuration. We measured second-order autocorrelation photon statistics of the emitters with a free-space Hanbury Brown Twiss (HBT) interferometer and detection using fiber-coupled Excelitas avalanche photodiodes (APDs). To measure the excited state lifetime of single emitters, we used time-correlated single photon counting (PicoHarp 300) and a pulsed laser source (SuperK). For low-temperature measurements, we used a closed-cycle helium cryostat with a base temperature of 4 K (Montana Instruments) with a built-in objective (NA = 0.9) and detection using free-space Excelitas APDs for confocal microscopy. Spectra were taken with a Princeton Instruments Isoplane SCT320 spectrometer with a resolution of 0.07 ± 0.01 nm. A third confocal microscope setup with NA = 1.3 oil-immersion microscope objective and free-space APDs was used for high efficiency collection measurements.

PIC to Fiber Edge Coupling. Our edge coupler design was not optimized to mode match with the UHNA3 fiber, which is multimode at our wavelengths of interest. The theoretical out-coupling efficiency into the fundamental fiber mode from the 450 nm × 200 nm AlN waveguide is on average 32% for over the span of 590 to 690 nm in wavelength when coupled optimally for 640 nm; there is also 2% coupling into higher order modes. The theoretical efficiency was calculated using 3D Finite-Difference Time-Domain (FDTD) method (Lumerical Inc.). We expect the experimental coupling efficiency to be less than 7% due to it being sensitive to the edge coupler polishing quality.[28] Experimentally, we placed a half-wave plate before the objective of the confocal microscope in order to minimize the laser coupling into the waveguide mode.

■ ASSOCIATED CONTENT

Supporting Information

The Supporting Information is available free of charge at https://pubs.acs.org/doi/10.1021/acsphotonics.0c01259.

Zoomed-in view of second-order autocorrelation histograms (PDF)

■ AUTHOR INFORMATION

Corresponding Authors

Dirk Englund − *Department of Electrical Engineering and Computer Science, Massachusetts Institute of Technology, Cambridge, Massachusetts 02139, United States;* orcid.org/0000-0002-1043-3489; Email: englund@mit.edu

Tsung-Ju Lu − *Department of Electrical Engineering and Computer Science, Massachusetts Institute of Technology, Cambridge, Massachusetts 02139, United States;* orcid.org/0000-0002-8644-9401; Email: tsungjul@mit.edu

Authors

Benjamin Lienhard − *Department of Electrical Engineering and Computer Science, Massachusetts Institute of Technology, Cambridge, Massachusetts 02139, United States*

Kwang-Yong Jeong − *Department of Electrical Engineering and Computer Science, Massachusetts Institute of Technology, Cambridge, Massachusetts 02139, United States*

Hyowon Moon − *Department of Electrical Engineering and Computer Science, Massachusetts Institute of Technology, Cambridge, Massachusetts 02139, United States*

Ava Iranmanesh − *Department of Electrical Engineering and Computer Science, Massachusetts Institute of Technology, Cambridge, Massachusetts 02139, United States*

Gabriele Grosso − *Photonics Initiative, Advanced Science Research Center and Physics Program, Graduate Center, City University of New York, New York, New York 10031, United States;* orcid.org/0000-0002-2577-1755

Complete contact information is available at: https://pubs.acs.org/10.1021/acsphotonics.0c01259

Author Contributions

‡These authors contributed equally to this work.

Notes

The authors declare no competing financial interest.

■ ACKNOWLEDGMENTS

This work was supported in part by the Army Research Office MURI (Ab-Initio Solid-State Quantum Materials) Grant No. W911NF-18-1-0431 and in part by National Science Foundation (NSF) Research Advanced by Interdisciplinary Science and Engineering (RAISE), Grant No. CHE-1839155. T.-J.L. acknowledges support from the Department of Defense National Defense Science and Engineering Graduate Fellowship as well as the Air Force Research Laboratory RITA Program FA8750-16-2-0141. B.L. acknowledges support from Center for Integrated Quantum Materials (CIQM). K.-Y.J. acknowledges support from the National Research Foundation of Korea (NRF) Grant funded by the Korean government (MSIT; 2015R1A6A3A03020926 and 2018R1D1A1B07043390). H.M. acknowledges support from the Samsung Scholarship as well as partial support from the NSF RAISE TAQS program. A.I. acknowledges support by the MIT UROP program. G.G. acknowledges support from the Graduate Center of the City University of New York (CUNY) through start-up funding.

■ REFERENCES

(1) Awschalom, D. D.; Hanson, R.; Wrachtrup, J.; Zhou, B. B. Quantum technologies with optically interfaced solid-state spins. *Nat. Photonics* **2018**, *12*, 516−527.

(2) Atatüre, M.; Englund, D.; Vamivakas, N.; Lee, S.-Y.; Wrachtrup, J. Material platforms for spin-based photonic quantum technologies. *Nature Reviews Materials* **2018**, *3*, 38−51.

(3) Doherty, M. W.; Manson, N. B.; Delaney, P.; Jelezko, F.; Wrachtrup, J.; Hollenberg, L. C. L. The nitrogen-vacancy colour centre in diamond. *Phys. Rep.* **2013**, *528*, 1−45.

(4) Trusheim, M. E.; et al. Transform-Limited Photons From a Coherent Tin-Vacancy Spin in Diamond. *Phys. Rev. Lett.* **2020**, *124*, 023602.

(5) Siyushev, P.; et al. Optical and microwave control of germanium-vacancy center spins in diamond. *Phys. Rev. B: Condens. Matter Mater. Phys.* **2017**, *96*, No. 081201.
(6) Becker, J.; Becher, C. Coherence Properties and Quantum Control of Silicon Vacancy Color Centers in Diamond. *Phys. Status Solidi A* **2017**, *214*, 1700586.
(7) Trusheim, M. E.; Wan, N. H.; Chen, K. C.; Ciccarino, C. J.; Flick, J.; Sundararaman, R.; Malladi, G.; Bersin, E.; Walsh, M.; Lienhard, B.; Bakhru, H.; Narang, P.; Englund, D. Lead-related quantum emitters in diamond. *Phys. Rev. B: Condens. Matter Mater. Phys.* **2019**, *99*, 075430.
(8) Lienhard, B.; Schröder, T.; Mouradian, S.; Dolde, F.; Tran, T. T.; Aharonovich, I.; Englund, D. Bright and photostable single-photon emitter in silicon carbide. *Optica* **2016**, *3*, 768−774.
(9) Castelletto, S.; Johnson, B. C.; Ivády, V.; Stavrias, N.; Umeda, T.; Gali, A.; Ohshima, T. A silicon carbide room-temperature single-photon source. *Nat. Mater.* **2014**, *13*, 151−156.
(10) Wolfowicz, G.; Anderson, C. P.; Diler, B.; Poluektov, O. G.; Heremans, F. J.; Awschalom, D. D. Vanadium spin qubits as telecom quantum emitters in silicon carbide. *Science Advances* **2020**, *6*, No. eaaz1192.
(11) Weber, J. R.; Koehl, W. F.; Varley, J. B.; Janotti, A.; Buckley, B. B.; Van de Walle, C. G.; Awschalom, D. D. Quantum computing with defects. *Proc. Natl. Acad. Sci. U. S. A.* **2010**, *107*, 8513−8518.
(12) Wehner, S.; Elkouss, D.; Hanson, R. Quantum internet: A vision for the road ahead. *Science* **2018**, *362*, No. eaam9288.
(13) Zaiser, S.; Rendler, T.; Jakobi, I.; Wolf, T.; Lee, S.-Y.; Wagner, S.; Bergholm, V.; Schulte-Herbruggen, T.; Neumann, P.; Wrachtrup, J. Enhancing quantum sensing sensitivity by a quantum memory. *Nat. Commun.* **2016**, *7*, 12279.
(14) Tran, T. T.; Bray, K.; Ford, M. J.; Toth, M.; Aharonovich, I. Quantum emission from hexagonal boron nitride monolayers. *Nat. Nanotechnol.* **2016**, *11*, 37−41.
(15) Berhane, A. M.; Jeong, K.; Bodrog, Z.; Fiedler, S.; Schröder, T.; Triviño, N. V.; Palacios, T.; Gali, A.; Toth, M.; Englund, D.; Aharonovich, I. Bright Room-Temperature Single-Photon Emission from Defects in Gallium Nitride. *Adv. Mater.* **2017**, *29*, 1605092.
(16) Lienhard, B.; Lu, T.-J.; Jeong, K.-Y.; Moon, H.; Iranmanesh, A.; Grosso, G.; Englund, D. High-Purity Single Photon Emitter in Aluminum Nitride Photonic Integrated Circuit. *European Conference on Lasers and Electro-Optics and European Quantum Electronics Conference, EA_6_6*, Germany, 2017, OSA Publishing, 2017
(17) Kim, S.; Duong, N. M. H.; Nguyen, M.; Lu, T.; Kianinia, M.; Mendelson, N.; Solntsev, A.; Bradac, C.; Englund, D. R.; Aharonovich, I. Integrated on Chip Platform with Quantum Emitters in Layered Materials. *Adv. Opt. Mater.* **2019**, *7*, 1901132.
(18) Seo, H.; Govoni, M.; Galli, G. Design of defect spins in piezoelectric aluminum nitride for solid-state hybrid quantum technologies. *Sci. Rep.* **2016**, *6*, 20803.
(19) Maity, S.; Shao, L.; Bogdanović, S.; Meesala, S.; Sohn, Y.-I.; Sinclair, N.; Pingault, B.; Chalupnik, M.; Chia, C.; Zheng, L.; Lai, K.; Lončar, M. Coherent acoustic control of a single silicon vacancy spin in diamond. *Nat. Commun.* **2020**, *11*, 193.
(20) Xiong, C.; Pernice, W. H. P.; Sun, X.; Schuck, C.; Fong, K. Y.; Tang, H. X. Aluminum nitride as a new material for chip-scale optomechanics and nonlinear optics. *New J. Phys.* **2012**, *14*, 095014.
(21) Harris, J. H. Sintered aluminum nitride ceramics for high-power electronic applications. *JOM* **1998**, *50*, 56−60.
(22) Hou, Y.; Zhang, M.; Han, G.; Si, C.; Zhao, Y.; Ning, J. A review: Aluminum nitride MEMS contour-mode resonator. *J. Semicond.* **2016**, *37*, 101001.
(23) Feneberg, M.; Leute, R. A. R.; Neuschl, B.; Thonke, K.; Bickermann, M. High-excitation and high-resolution photoluminescence spectra of bulk AlN. *Phys. Rev. B: Condens. Matter Mater. Phys.* **2010**, *82*, 075208.
(24) Xiong, C.; Pernice, W. H. P.; Tang, H. X. Low-Loss, Silicon Integrated, Aluminum Nitride Photonic Circuits and Their Use for Electro-Optic Signal Processing. *Nano Lett.* **2012**, *12*, 3562−3568.
(25) Lu, T.-J.; Fanto, M.; Choi, H.; Thomas, P.; Steidle, J.; Mouradian, S.; Kong, W.; Zhu, D.; Moon, H.; Berggren, K.; Kim, J.; Soltani, M.; Preble, S.; Englund, D. Aluminum nitride integrated photonics platform for the ultraviolet to visible spectrum. *Opt. Express* **2018**, *26*, 11147−11160.
(26) Guo, X.; Zou, C.-L.; Schuck, C.; Jung, H.; Cheng, R.; Tang, H. X. Parametric down-conversion photon-pair source on a nanophotonic chip. *Light: Sci. Appl.* **2017**, *6*, No. e16249.
(27) Jung, H.; Tang, H. X. Aluminum nitride as nonlinear optical material for on-chip frequency comb generation and frequency conversion. *Nanophotonics* **2016**, *5*, 263−271.
(28) Wan, N. H.; Lu, T.-J.; Chen, K. C.; Walsh, M. P.; Trusheim, M. E.; De Santis, L.; Bersin, E. A.; Harris, I. B.; Mouradian, S. L.; Christen, I. R.; Bielejec, E. S.; Englund, D. Large-scale integration of artificial atoms in hybrid photonic circuits. *Nature* **2020**, *583*, 226−231.
(29) Berger, L. I. *Semiconductor Materials*; CRC Press, 1996.
(30) Silfvast, W. T. *Laser Fundamentals*; Cambridge University Press, 1996.
(31) Neu, E.; Agio, M.; Becher, C. Photophysics of single silicon vacancy centers in diamond: implications for single photon emission. *Opt. Express* **2012**, *20*, 19956−19971.
(32) Hizhnyakov, V.; Reineker, P. Optical dephasing by fluctuations of long-range interactions in defect-rich crystals. *J. Lumin.* **1999**, *83*−*84*, 351−355.
(33) Kitson, S. C.; Jonsson, P.; Rarity, J. G.; Tapster, P. R. Intensity fluctuation spectroscopy of small numbers of dye molecules in a microcavity. *Phys. Rev. A: At., Mol., Opt. Phys.* **1998**, *58*, 620.
(34) Aharonovich, I.; Castelletto, S.; Johnson, B. C.; McCallum, J. C.; Simpson, D. A.; Greentree, A. D.; Prawer, S. Chromium single-photon emitters in diamond fabricated by ion implantation. *Phys. Rev. B: Condens. Matter Mater. Phys.* **2010**, *81*, No. 121201.
(35) Xue, Y.; Wang, H.; Xie, N.; Yang, Q.; Xu, F.; Shen, B.; Shi, J.-J.; Jiang, D.; Dou, X.; Yu, T.; Sun, B.-Q. Single-Photon Emission from Point Defects in Aluminum Nitride Films. *J. Phys. Chem. Lett.* **2020**, *11*, 2689−2694.
(36) Bishop, S. G.; Hadden, J. P.; Alzahrani, F. D.; Hekmati, R.; Huffaker, D. L.; Langbein, W. W.; Bennett, A. J. Room-Temperature Quantum Emitter in Aluminum Nitride. *ACS Photonics* **2020**, *7*, 1636−1641.
(37) Grosso, G.; Moon, H.; Ciccarino, C.; Flick, J.; Mendelson, N.; Mennel, L.; Toth, M.; Aharonovich, I.; Narang, P.; Englund, D. R. Low-Temperature Electron−Phonon Interaction of Quantum Emitters in Hexagonal Boron Nitride. *ACS Photonics* **2020**, *7*, 1410−1417.
(38) Miao, J.; Ercius, P.; Billinge, S. J. L. Atomic electron tomography: 3D structures without crystals. *Science* **2016**, *353*, aaf2157.
(39) Zhu, D.; Zhao, Q.-Y.; Choi, H.; Lu, T.-J.; Dane, A. E.; Englund, D.; Berggren, K. K. A scalable multi-photon coincidence detector based on superconducting nanowires. *Nat. Nanotechnol.* **2018**, *13*, 596−601.
(40) Guo, X.; Zou, C.-L.; Jung, H.; Tang, H. X. On-Chip Strong Coupling and Efficient Frequency Conversion between Telecom and Visible Optical Modes. *Phys. Rev. Lett.* **2016**, *117*, 123902.
(41) Bi, W.; Kuo, H.; Ku, P.; Shen, B. *Handbook of GaN Semiconductor Materials and Devices*; CRC Press, 2017.
(42) Nagasawa, Y.; Hirano, A. A Review of AlGaN-Based Deep-Ultraviolet Light-Emitting Diodes on Sapphire. *Appl. Sci.* **2018**, *8*, 1264.
(43) Popa, L. C.; Weinstein, D. Switchable piezoelectric transduction in AlGaN/GaN MEMS resonators. *Transducers & Eurosensors XXVII: The 17th International Conference on SolidState Sensors Actuators and Microsystems* **2013**, 2461−2464.
(44) Grosso, G.; Moon, H.; Lienhard, B.; Ali, S.; Efetov, D. K.; Furchi, M. M.; Jarillo-Herrero, P.; Ford, M. J.; Aharonovich, I.; Englund, D. Tunable and high-purity room temperature single-photon emission from atomic defects in hexagonal boron nitride. *Nat. Commun.* **2017**, *8*, 705.

https://dx.doi.org/10.1021/acsphotonics.0c01259
ACS Photonics 2020, 7, 2650−2657